Palynological record of the Carnian Pluvial Episode from the northwestern Sichuan Basin, SW China

Liqin Li, Wolfram M. Kürschner, Ning Lu, Hongyu Chen, Pengcheng An, Yongdong Wang

PII: S0034-6667(22)00102-6

DOI: https://doi.org/10.1016/j.revpalbo.2022.104704

Reference: PALBO 104704

To appear in: *Review of Palaeobotany and Palynology*

Received date: 10 January 2022

Revised date: 31 May 2022

Accepted date: 2 June 2022

Please cite this article as: L. Li, W.M. Kürschner, N. Lu, et al., Palynological record of the Carnian Pluvial Episode from the northwestern Sichuan Basin, SW China, *Review of Palaeobotany and Palynology* (2021), https://doi.org/10.1016/j.revpalbo.2022.104704

Palynological record of the Carnian Pluvial Episode from the northwestern Sichuan Basin, SW China

Liqin Li [a], Wolfram M. Kürschner [b], Ning Lu [a], Hongyu Chen [a], Pengcheng An [a], Yongdong Wang [a,*]

[a] State Key Laboratory of Palaeobiology and Stratigraphy, Nanjing Institute of Geology and Palaeontology, and Center for Excellence in Life and Paleoenvironment, Chinese Academy of Sciences, East Beijing Road 39, Nanjing 210008, China

[b] Department of Geosciences, University of Oslo, P.O. Box 1047, Blindern, 0316 Oslo, Norway

[*] Corresponding author: ydwang@nigpas.ac.cn (Y. Wang)

Abstract

The prevailing arid Late Triassic climate was interrupted by a humid Carnian Pluvial Episode (CPE) during the mid-Carnian period. In this study, a palynological study was conducted for the Ma'antang Formation (Carnian) from the northwestern Sichuan Basin, SW China, in the eastern Tethys. The study reveals dominance of terrestrial palynomorphs, and two palynological assemblage zones were identified. Palynofloras are well-presented by dominant ferns (especially Dipteridaceae/Matoniaceae), with less abundant lycopsids, conifers, cycadophytes/ginkgophytes and seed ferns. Overwhelming predominance of wet Lowland SEG and hygrophyte elements, and increased Lowland/Hinterland as well as hygrophyte/xerophyte ratios observed in Units 2-4 of the Ma'antang Formation, suggesting intensified humidity during the Julian 2 in this area.

This study presents the first palynological evidence for vegetation changes in South China during the CPE, and correlates well with observations from North China as well as western Tethys, thus further supports worldwide impact of humid climate associated with the CPE.

Keywords: Carnian Pluvial Episode; eastern Tethys; humid climate; palynology

1. Introduction

The Late Triassic Carnian Stage witnessed major global climatic changes and biotic turnover during the late Early to Late Carnian (Julian 2–Tuvalian), known as the "Carnian Pluvial Episode/Event" (CPE) (Simms and Ruffell, 1989; Roghi et al., 2010; Zhang et al., 2015; Miller et al., 2017; Dal Corso et al., 2018). The CPE is characterized by increased rainfall, humid and warmer climate (Simms and Ruffell, 1989; Hornung et al., 2007; Preto et al., 2010; Ruffell et al., 2016), carbon cycle perturbations (Hornung et al., 2007; Dal Corso et al., 2012, 2015, 2018; Sun et al., 2016; Miller et al., 2017; Li et al., 2021), demise of carbonate platforms and enhanced terrigenous clastic input (Rigo et al., 2007; Hornung et al., 2007; Stefani et al., 2010; Gattolin et al., 2015; Shi et al., 2017, 2019; Jin et al., 2018). This episode is also accompanied by high biotic extinction rates (including ammonites, bryozoa, conodonts, and crinoids) as well as diversifications (e.g. dinosaurs, scleractinian reefs, calcareous nanoplanktons, lepidosaurs, conifers) (Simms and Ruffell, 1989; Furin et al., 2006; Bernardi et al., 2018; Dal Corso et al., 2020). Negative carbon isotope excursions and increased mercury concentration (Dal Corso et al., 2012; Li et al., 2020; Lu et al., 2021; Mazaheri-Johari et al., 2021), along with other

geochemical proxies (Furin et al., 2006; Miller et al., 2017) suggest that the Wrangellia large igneous province (LIP) volcanism in the northeastern Pacific likely triggered the CPE, with massive release of volcanic CO_2 causing global warming, enhanced hydrological cycle and marine acidification.

Although persuasiveness of the evidence for this humid climate period and its global extent of the CPE has been debated (Visscher et al., 1994; Franz et al., 2019), a series of sedimentological studies from Europe (e.g. Kozur and Bachmann, 2010; Rostási et al., 2011; Arche and López-Gómez, 2014), North America (Preto et al., 2006) and Asia (Nakada et al., 2014; Sun et al., 2016) suggest global wetter conditions during the CPE (Ruffell et al., 2016). Palynological studies show increased abundance of hygrophyte plants through the CPE from the Boreal realm (Mueller et al., 2016a), northeastern margin of Tethys (Mazaheri-Johari et al., 2022) and western Tethys (e.g. Roghi, 2004; Roghi et al. 2010; Mueller et al., 2016b; Baranyi et al., 2019a; Fijałkowska-Mader et al., 2021). These findings suggest a widespread CPE humid climatic conditions, however, some palynological records did not show significant humidity signals, e.g. UK (Baranyi et al., 2019b) and Danish Basin (Lindström et al., 2017).

In East Asia, an increase of hygrophytic spores and carbon isotope excursions were recently reported from the Jiyuan Basin of North China during the CPE, indicating intensified humidity (Lu et al., 2021). Increased fern spores were also identified in the Junggar Basin, North China, likely records a regional response to the CPE (Peng et al., 2022). In South China, the Carnian negative carbon isotope excursions have been recognized in the Guizhou (Sun et al., 2016), Sichuan (Shi et al., 2019) and Hubei (Li et al., 2021) provinces, however palynological records of the CPE still remains poorly

documented.

In order to trace terrestrial response of the CPE in South China, here we present quantitative palynological data from the northwestern Sichuan Basin, SW China, and interpret the vegetation and palaeoclimatic condition in this special time interval of the Late Triassic.

2. Geological Setting and stratigraphy

The Sichuan Basin was located in the northwestern margin of the South China block, at the eastern Tethys, during the Triassic (Fig. 1A). In the Sichuan Basin, the late Proterozoic−Middle Triassic marine carbonate platforms are widely developed, while the Late Triassic and younger strata are mainly terrestrial origin (Wang et al., 2010). Collision between North China and South China plates at the late Middle Triassic caused extensive erosion of the Middle Triassic dolomites, and unconformity between the Middle and Upper Triassic sequences in the Sichuan Basin (Li et al., 2011). This collision also turned this area from a passive continental margin into the western Sichuan foreland Basin (Li et al., 2011).

Within the Sichuan Basin, the Upper Triassic (Carnian) Ma'antang Formation is only developed along the northwestern margin. This is owing to a semi-enclosed Western Sichuan Bay connected with the Palaeotethys Ocean, whereas most of South China was exposed (Deng et al., 1982; Wu, 1984). The Ma'antang Formation consists mainly of oolitic, bioclastic and sponge-mound limestone in the lower part, while the upper part is mainly composed of dark shale interbedded with grey siltstone and few limestone beds, with a coarsening upward trend (Shi et al., 2017, 2019). Conodonts and ammonites found

in the Ma'antang Formation constrain its age as Carnian (Shi et al., 2017, 2019; Jiang et al., 2019). Recent ammonite biostratigraphy and detrital zircon U/Pb studies suggest that, the Ma'antang Formation may also include Norian sediments in the upper part at some sections (Jin et al., 2019; Mietto et al., 2021).

At the Ma'antang section (type section of the Ma'antang Formation), about 70 km northeastward from Jiangyou City, northwestern Sichuan Basin (Fig. 1B-C), the Ma'antang Formation unconformably overlays the Middle Triassic Tianjingshan Formation, and in turn is conformably overlain by the Upper Triassic Xiaotangzi Formation (Norian) (Wu, 1989; Fig. 2). In this section, the Ma'antang Formation is about 200 m thick, and was divided into five lithological units by Shi et al. (2019). The Units 1−3 consists mainly of bioclastic limestone interbedded with silty mudstone, whereas the Units 4−5 are mainly muddy siltstone, silty mudstone, sandstone and bioclastic limestone (Fig. 2; Shi et al., 2019). Ammonite and conodont fossils imply that Units 2−4 and Unit 5 are Julian 2 and Tuvalian in age, respectively (Shi et al., 2019; Fig. 2). Negative carbon isotope excursion observed in upper Unit 1 to Unit 4, accompanied by input of terrigenous sediments (shale and siltstone), were suggested as records of the CPE event in this area (Shi et al., 2019; Jin et al., 2020).

Lu and Wang (1980) firstly identified the *Corollisporites-Micrhystridium* palynological assemblage from the Ma'antang Formation at the Ma'antang Section, and roughly suggested it as Carnian in age (Lu and Wang, 1987). However, owing to lack of detailed sample horizons and quantitative data, the CPE-related palynological response and palaeovegetation as well as palaeoclimate conditions still remain poorly known.

3. Material and Methods

A total of 23 palynological samples were collected from siltstones and shales within the Ma'antang Formation at the Ma'antang section, Jiangyou City (Fig. 2). Palynological samples were crushed and treated with HCl (30%) and HF (38%) to remove the carbonate and silicate minerals. After washing and sieving (10 μm mesh), residues were mounted onto slides using glycerin jelly and sealed with paraffin wax. Palynological treatment was performed at the Nanjing Institute of Geology and Palaeontology, Chinese Academy of Sciences (NIGPAS). All samples and slides are housed at NIGPAS.

Spore and pollen identification was based on Song et al. (2000), which summarized all published Mesozoic spore and pollen taxa of China, and acritarchs were identified referring to Van Soelen and Kürschner (2018). More than 200 terrestrial palynomorphs, where possible, were counted for each sample (Table S1) with a Leica DM 1000 microscope, and photographed using a SC1200 microscope imaging system. Aquatic palynomorphs (including acritarch and foraminiferal test lining) were excluded in the quantitative palynological analysis. Relative spore and pollen abundances were calculated and plotted using the Tilia/TiliaGraph computer program (Grimm, 2004). Palynological assemblages were identified by stratigraphically constrained cluster analysis (CONISS) within the Tilia (Grimm, 2004).

The palaeovegetation interpretations were carried out based on known or probable major botanical affinities of dispersed spores and pollen (Van Konijnenburg-Van Cittert, 1971, 1993; Litwin, 1985, Balme, 1995; Wang and Zhang, 2010; Mander et al., 2012; Bonis and Kürschner, 2012; Wang et al., 2015; Lindström, 2016; Baranyi et al., 2019b; Li et al., 2018, 2020; Nowak et al., 2022) (Table 1). The classification of spores and

pollen taxa as hygrophyte, intermediate and xerophyte groups follows the concept of Visscher and Van der Zwan (1981), based on morphological group of spores and pollen (Table 1). The Sporomorph Ecogroup Model (SEG) method, which link dispersed spores and pollen with plant communities labelled as ecogroups (Abbink et al., 2004), was applied for the palaeoecological interpretation. Several published studies have supplied more detailed information on possible ecological preferences of Mesozoic plants and palynological taxa, and were referred here to assign spores and pollen into SEG groups (e.g. Van Konijnenburg-Van Cittert, 2002; Kustatscher et al., 2012; Baranyi et al., 2019b; Li et al., 2020) (Table 1).

4. Result

4.1 Palynology

Fourteen out of 23 processed samples from the Ma'antang Formation at the Ma'antang section are productive (Fig. 2), and contain diverse and well-preserved palynomorphs. A total of 83 terrestrial spore and pollen taxa and five aquatic acritarch taxa were identified. The representative palynomorphs are illustrated in Plates I-III. All identified taxa and original count data are listed in Table S1.

The palynomorph assemblages of Ma'antang Formation in the studied section are dominated by terrestrial spores and pollen for most samples (Fig. 2). Amongst, trilete spores are the most abundant group (68–96%), bisaccate pollen (1–27%), monosulcate pollen (1–4%) and monolete spores (0–2%) occupy minor proportions. Two palynological assemblages were distinguished by cluster analysis (CONISS) (Fig. 2).

4.1.1 Palynological Assemblage A

The Assemblage A occurs in the Units 1–2 of the Ma'antang Formation (samples MAT-1 to MAT-4), and is characterized by co-dominance of *Kyrtomisporis* (*K. coronaries*, *K. laevigatus*, *K. speciosus*) (11–45%), *Dictyophyllidites* (*D. charicis*, *D. harrisii*, *D. mortoni*, *D. intercrassus*) (10–41%) and *Concavisporites* (*C. toralis*, *C. bohemiensis*, *C. kermanense*) (4–23%) (Fig. 2; Table S1). Common trilete spores include *Granulatisporites*, *Uvaesporites*, *Canalizonospora*, *Asseretospora* and *Kraeuselisporites* (Fig. 2; Table S1). Other trilete spores occurring in lower abundances (<3%) include *Deltoidospora*, *Cyathidites*, *Punctatisporites*, *Calamospora*, *Cyclogranisporites pressus*, *Osmundacidites*, *Conbaculatisporites*, *Lycopodiacidites*, *Habrozonosporites* and *Annulispora* (Fig. 2; Table S1). Other spore and pollen groups constitute minor proportions in the palynological assemblages, such as alete bisaccate pollen (2–19%) (*Caytonipollenites*, *Alisporites*, *Pinuspollenites*, *Cedripites*, *Quadraeculina*, *Podocarpidites*, *Granosaccus*, *Verrusaccus*), striate bisaccate pollen (<5%) (*Taeniaesporites*, *Lueckisporites*, *Protohaploxypinus*), monosulcate pollen (2–4%) (*Cycadopites*, *Chasmatosporites*, *Monosulcites*), monolete spores (<1%) (*Aratrisporites*, *Laevigatosporites*) and alete pollen (<2%) (*Araucariacites*) (Table S1). *Cerebropollenites*, *Ricciisporites tuberculatus* and *Ovalipollis ovalis* show sporadic occurrences (Table S1).

Aquatic palynomorphs have low numbers (4–25%), except for the lowermost sample (95%) (Fig. 2), mainly represented by marine acritarchs *Micrhystridium* and *Veryhachium*, with a few *Granoreticella* and foraminiferal test linings distinguished (Table S1).

The above palynological composition in the Units 1–2 of the Ma'antang Formation is consistent with those reported by Lu and Wang (1980), revealing a *Kyrtomisporis* (we

regard *Corollisporites* in Lu and Wang (1980) as *Kyrtomisporis* in this study)–*Dictyophyllidites*–*Micrhystridium* palynological assemblage during the early Julian 2 in the Sichuan Basin.

4.1.2 Palynological Assemblage B

The Assemblage B in the Units 4–5 of the Ma'antang Formation (samples MAT-11 to MAT-23) is characterized by significant dominance of *Granulatisporites* (*G. granulatus*, *G. parvus*) (16–48%), decrease of *Kyrtomisporis* (<2%), common occurrence of *Dictyophyllidites* (*D. charicis*, *D. harrisii*, *D. mortoni*, *D. intercrassus*) (2–22%), *Lunzisporites* (*L. lunzensis*, *L. delicatulus*) (5–19%) and *Concavisporites* (*C. toralis*, *C. bohemiensis*, *C. kermanense*) (5–16%) (Fig. 2; Table S1). Less common trilete spores mainly include *Cyathidites*, *Deltoidospora*, *Punctatisporites*, *Calamospora*, *Cyclogranisporites*, *Osmundacidites*, *Anapiopteridaspora*, *Planisporites*, *Baculatisporites* and *Conbaculatisporites* (Fig. 2; Table S1). Monolete spores (*Laevigatosporites*, *Marattisporites*, *Aratrisporites*) are rare (<2%) (Table S1). Gymnosperm pollen are much less abundant (5–32%), and represented by bisaccate pollen (3–27%) (*Taeniaesporites*, *Lueckisporites*, *Protohaploxypinus*, *Caytonipollenites*, *Alisporites*, *Pinuspollenites*, *Paleoconiferus*, *Podocarpidites*) and monosulcate pollen (1–4%) (*Chasmatosporites*, *Cycadopites*, *Monosulcites*).

Trilete spores decrease from the Unit 4 (82–96%) towards the Unit 5 (68%), while bisaccate pollen increase from 3–11% within the Unit 4 to 27% in the Unit 5 (Table S1).

Aquatic palynomorphs including marine acritarchs *Micrhystridium*, *Veryhachium*, *Baltisphaeridium*, *Leiopsophosphaera*, *Granoreticella* and foraminiferal test linings (Table S1).

The present Ma'antang palynofloras resemble the AZ-II of the Jiyuan Basin (Lu et al., 2021) and the Palynoflora C from the Junggar Basin (Peng et al., 2022) in dominance of fern spores, shared taxa include *Dictyophyllidites*, *Osmundacidites*, *Cyclogranisporites*, *Baculatisporites*, *Kraeuselisporites*, *Laevigatosporites*, *Calamospora*, *Chasmatosporites* and *Cycadopites*. The Ma'antang palynoflora have even higher abundance and diversity of fern spores than the other two assemblages from the Jiyuan and Junggar basins in North China. Dominant spores in the lower Ma'antang palynoflora (Assemblage A) mainly include laevis azonotrilete (*Dictyophyllidites*, *Concavisporites*) and zonotrilete (*Kyrtomisporis*) types. Both the upper Ma'antang palynoflora (Assemblage B) and coeval palynofloras in North China mainly consist of apiculate and laevis azonotrilete spores, but they were represented by different dominant taxa. The former mainly includes *Granulatisporites*, *Lunzisporites*, *Dictyophyllidites* and *Concavisporites*, whereas the latter mainly includes *Osmundacidites*, *Cyclogranisporites*, *Apiculatisporis*, *Punctatisporites*, *Todisporites* and *Leiotriletes* (Lu et al., 2021; Peng et al., 2022). This may reflect difference between two separate Late Triassic floristic provinces, the Ma'antang belonged to the South China Floristic Region, while the Jiyuan and Junggar were parts of the North China Floristic Region (Sun, 1995).

4.2 Palaeovegetation profile

Based on the botanical affinity of the dispersed spores and pollen recovered from the Ma'antang Formation (Table 1), Carnian vegetation profile of the Ma'antang region was reconstructed. The vegetation can be described as a lowland mire forest. Ferns are predominant type throughout the section (66–91%), and represented by

Dipteridaceae/Matoniaceae (15−83%), also with less abundant Osmundaceae and Marattiales, and a few Pteridaceae (Fig. 3). Lycopsids are abundant in the Unit 2 (early Julian 2) (6−16%) and decrease in younger strata (1-4%) (Fig. 3). Ferns, lycopsids together with a few mosses and horsetails, making up the ground cover vegetation. Mid-canopy seed ferns and upper canopy conifers trees account for relatively low percentages in the Units 2–4 (1–8%), but have higher abundance in the uppermost Unit 1 and Unit 5 (11–18%) (Fig. 3). Mid-canopy cycadophytes/ginkgophytes trees are less abundant (1–4%) in this flora (Fig. 3).

4.3 Palaeoclimatic interpretation

In the present study, four terrestrial SEGs were distinguished: wet and dry Lowland SEG, River SEG, and Hinterland SEG (Table 1; Fig. 4). The wet Lowland SEG represents plant communities growing in marshes and swamps, the dry Lowland SEG reflects floodplain vegetation occasionally submerged, the River SEG refers to riverbank communities (Abbink et al., 2004), and the hinterland SEG reflects plant communities on well-drained terrains above groundwater table (Kustatscher et al., 2012). The application of the SEG method reveals a highly dominance of wet Lowland SEG (68−91%) and less abundant River SEG (5−17%), the dry Lowland and Hinterland SEGs are minor constituents (Fig. 4). This implies a generally humid lowland marsh ecosystem in the western Sichuan Basin during the Carnian period. Higher abundances of Lowland SEG and lower percentages of Hinterland SEG in the Units 2–4 result in peaks in the Lowland/Hinterland ratio (Fig. 4), suggesting intensification of humidity during the Julian 2.

Hygrophyte-xerophyte analysis shows a marked predominance of sporopollen attributed to hygrophyte group (ferns, horsetails, lycopsids, mosses and seed ferns) (80−98%), xerophyte (conifers) (1−16%) and intermediate (cycadophytes/ginkgophytes, Araucariaceae and Taxodiaceae) (1−6%) elements are much less common (Fig. 4). Hygrophyte/xerophyte ratio shows similar curve with the Lowland/Hinterland ratio, higher hygrophyte/xerophyte ratios and absolute predominance of hygrophyte elements (>90%) in the Units 2–4 (Fig. 4) suggest extremely humid climate during the mid-Carnian (Julian 2) in the western Sichuan Basin.

5. Discussion

Multiple negative carbon isotope excursions (NCIEs) have been globally recognized during the CPE, from marine, paralic and terrestrial successions (Sun et al., 2016; Miller et al., 2017; Dal Corso et al., 2018, Baranyi et al., 2019b; Li et al., 2021; Lu et al., 2021; Tomimatsu et al., 2021). Biostratigraphy and carbon-isotope correlation implies that NCIEs punctuate the entire CPE (Dal Corso et al., 2018). Amongst, the NCIE-1 at the Julian 1−Julian 2 boundary marks the onset of the CPE, and the NCIE-3 occurs at the Julian–Tuvalian boundary (Dal Corso et al., 2015, 2018, 2020; Sun et al., 2016; Shi et al., 2019). A long-lasting negative organic CIE was identified in the Ma'antang Formation at Ma'antang Section (Shi et al., 2019), and is similar to the one recorded at the Nanpanjiang Basin in South China, but where the carbonate carbon-isotope data seems to record three negative CIEs (Sun et al., 2016) (Fig. 5). Combined with ammonite-conodont biostratigraphy as well as carbonate carbon-isotope curve, the lower part of prolonged negative CIE in South China was correlated with the NCIE-1~3 of western

Tethys during the Julian 2 (Dal Corso et al., 2018; Shi et al., 2019) (Fig. 5). Major organic CIEs identified from the Jiyuan Basin, North China were well-correlated with western Tethys NCIE records (Lu et al., 2021; Fig. 5).

The observed predominance of ferns and increased hygrophyte/xerophyte ratios within the broad negative CIE during the Julian 2 at Ma'antang Section, show a close resemblance to those observed in coeval sediments at North China and elsewhere in eastern and western Tethys regions. An intensification of humidity was recorded in the Jiyuan Basin of North China, as suggested by co-dominance of freshwater algae and fern spores, and increased hygrophyte/xerophyte ratios, within the negative CIEs interval during the Julian 2 to early Tuvalian (Lu et al., 2021; Fig. 5). In the Junggar Basin of northwestern China, a shift from a conifer-dominated forest community to a fern-dominated community was recorded in the Huangshanjie Formation, and is interpreted as signal of increased humidity associated with the CPE (Peng et al., 2022). In the Aghdarband Basin of NE Iran, remarkable dominance of hygrophytic sporomorphs and coal layers were reported from the lowermost Miankuhi Formation, indicating relative humid palaeoclimate during the Julian 2 (Mazaheri-Johari et al., 2022).

Several palynological studies have been carried out for the CPE deposits in western Tethys. In the Transdanubian Range of western Hungary, elevated hygrophyte/xerophyte ratios and kaolinite contents were documented within the NCIE-1~NCIE-3 interval, indicating intensive terrestrial runoff and increased humidity during the Julian 2 (Dal Corso et al., 2018; Baranyi et al., 2019a) (Fig. 5). A humid climate condition was recorded in northeastern Italy by abundance of fern and lycopsid spores during the late Julian to the early Tuvalian (Roghi, 2004). Increases of hygrophyte sporomorphs

(including ferns, clubmoss, horsetails and cycads) and hygrophyte/xerophyte ratio were also revealed in the Julian 2 of Austria, indicating wetter climatic condition and widespread intensification of the hydrological cycle (Roghi et al., 2010; Mueller et al., 2016b) (Fig. 5). In Poland, the CPE is marked by a clear shift from xerophyte dominated microflora in the Garbfeld Formation to hygrophyte dominated one (horsetails, lycopsids and bennettitales) in the Stuttgart Formation, accompanied by palaeosol change from aridisols to poorly drained hydric soils, implying wetter climate (Fijałkowska-Mader et al., 2021). The missing humid CPE signal in the Danish Basin and the Wessex Basin, UK, may owe to too dry local condition in the inner inland or overrepresentation of xerophyte hinterland plants (Lindström et al., 2017; Baranyi et al., 2019b).

In the boreal realm, dominance of spores and occurrence of coal beds characterize the De Geerdalen Formation (late Julian) of Spitsbergen, Norway, suggesting a humid setting (Hounslow et al., 2007; Mueller et al., 2016a).

Carnian macroflora in South China are well-represented by the Daqiaodi flora in Sichuan-Yunnan area and Junggang flora in Hubei, and mainly include sphenophytes and ferns, and also common seed ferns and cycads/bennettitaleans (Zhou and Zhou, 1983; Kustatscher et al., 2018). The Lunz flora in Austria (Julian-2), a representative Carnian macrofloras in Europe, is characterized by abundance of ferns and cycads/bennettitaleans, less common occurrence of sphenophytes, and rare ginkgophytes and conifers, reflecting generally humid swampy fluvial to deltaic environments (Dobruskina, 1998; Pott et al., 2008; Mueller et al., 2016b; Kustatscher et al., 2018).

These widely reported palynological and macrofloral records suggest a global nature of the CPE. The coincidence of Hg concentration peaks, negative CIEs and warming

support LIP (probably Wrangellia) volcanism as trigger for the CPE (Sun et al., 2016; Lu et al., 2021; Mazaheri-Johari et al., 2021). LIP volcanism injected large volumes of ^{13}C-depleted CO_2 into atmosphere-ocean system, resulting in perturbations of the carbon cycle represented by CIE, warming climate, intensified hydrological cycle, increased precipitation and a consequent enhanced continental runoff during the CPE (Mueller et al., 2016a; Sun et al., 2016; Dal Corso et al., 2012, 2018, 2020; Lu et al., 2021).

6. Conclusions

This study records a CPE-related palynological signal in the eastern Tethyan succession of the western Sichuan Basin, South China. Terrigenous clastics in the Ma'antang Formation at Ma'antang Section yield diverse and well-preserved sporomorphs, and the palynoflora is predominated by fern (represented by Dipteridaceae/Matoniaceae). Dominance of wet Lowland SEG and hygrophyte elements through the section suggest a general humid lowland ecosystem in the western Sichuan Basin during the Carnian. Overwhelming predominance of wet Lowland SEG and hygrophyte elements, and increased hygrophyte/xerophyte ratios in the Units 2–4 reveal an extremely humid setting during the Julian 2 in the Sichuan Basin. The present study provides the first terrestrial palynological evidence of the CPE in South China. Correlation of palynological and carbon isotope data between eastern and western Tethys further supports a global nature of the CPE.

Acknowledgements

We thank Limei Feng for laboratory sample processing. Mihai E. Popa and Evelyn Kustatscher are acknowledged for their thorough reviews and constructive comments, which helped to improve the manuscript. This research was supported by the National Science Foundation of China [grant numbers 42072009, 41702004, 41790454, 41688103], the Strategic Priority Program (B) of CAS [grant numbers XDB18000000, XDB26000000], and the State Key Laboratory of Palaeobiology and Stratigraphy [grant numbers 20172103, 20191103, 213112].

References

Abbink, O.A., Van Konijnenburg-Van Cittert, J.H.A., Visscher, H., 2004. A sporomorphs ecogroup model for the Northwest European Jurassic - Lower Cretaceous I: Concepts and framework. Netherlands J. Geosci./Geol. Mijnbouw 83, 17–38.

Arche, A., López-Gómez, J., 2014. The Carnian Pluvial Event in Western Europe: new data from Iberia and correlation with the Western Neotethys and Eastern North America–NW Africa regions. Earth Sci. Rev. 128, 196–231.

Balme, B.E., 1995. Fossil in situ spores and pollen grains: An annotated catalogue. Rev. Palaeobot. Palynol. 87, 81–323.

Baranyi, V., Rostási, Á., Raucsik, B., Kürschner, W.M., 2019a. Palynology and weathering proxies reveal climatic fluctuations during the Carnian Pluvial Episode (CPE) (Late Triassic) from marine successions in the Transdanubian Range (western Hungary). Glob. Planet Change 177, 157–172.

Baranyi, V., Miller, C.S., Ruffell, A., Hounslow, M.W., Kürschner, W.M., 2019b. A continental record of the Carnian Pluvial Episode (CPE) from the Mercia Mudstone

Group (UK): palynology and climatic implications. J. Geol. Soc. London 176, 149–166.

Bernardi, M., Gianolla, P., Petti, F.M., Mietto, P., Benton, M.J., 2018. Dinosaur diversification linked with the Carnian Pluvial Episode. Nat. Commun. 9, 1499.

Bonis, N.R., Kürschner, W.M., 2012. Vegetation history, diversity patterns, and climate change across the Triassic/Jurassic boundary. Paleobiology 38, 240–264.

Dal Corso, J., Bernardi, M., Sun, Y.D., Song, H.J., Seyfullah, L.J., Preto, N., Gianolla, P., Ruffell, A., Kustatscher, E., Roghi, G., Merico, A., Hohn, S., Schmidt, A.R., Marzoli, A., Newton, R.J., Wignall, P.B., Benton, M.J., 2020. Extinction and dawn of the modern world in the Carnian (Late Triassic). Sci. Adv. 6, eaba0099.

Dal Corso, J., Gianolla, P., Newton, J.R., Franceschi, M., Roghi, G., Caggiati, M., Raucsik, B., Budai, T., Haas, J. Preto, N., 2015. Carbon isotope records reveal synchronicity between carbon cycle perturbation and the "Carnian pluvial event" in the Tethys realm (Late Triassic). Glob. Planet. Change 127, 79–90.

Dal Corso, J., Gianolla, P., Rigo, M., Franceschi, M., Roghi, G., Mietto, P., Manfrin, S., Raucsik, B., Budai, T., Jenkyns, H.C., Reymond, C.E., Caggiati, M., Gattolin, G., Breda, A., Merico, A., Preto, N., 2018. Multiple negative carbon-isotope excursions during the Carnian Pluvial Episode (Late Triassic). Earth Sci. Rev. 185, 732–750.

Dal Corso, J., Mietto, P., Newton, R.J., Pancost, R.D., Preto, N., Roghi, G., Wignall, P.B., 2012. Discovery of a major negative $\delta^{13}C$ spike in the Carnian (Late Triassic) linked to the eruption of Wrangellia flood basalts. Geology 40, 79–82.

Deng, K.L., He, L., Qin, D.Y., He, Z.G., 1982. The earlier late Triassic sequence and its sedimentary environment in western Sichuan basin. Oil Gas Geol. 3, 204–210 (in Chinese with English abstract).

Dobruskina, I.A., 1998. Lunz flora in the Austrian Alps—a standard for Carnian floras. Palaeogeogr. Palaeoclimatol. Palaeoecol. 143, 307–345.

Fijałkowska-Mader, A., Jewuła, K., Bodor, E., 2021. Record of the Carnian Pluvial Episode in the Polish microflora. Palaeoworld 30, 106–125.

Franz, M., Kustatscher, E., Heunisch, C., Niegel, S., Röhling, H.-G., 2019. The Schilfsandstein and its flora; arguments for a humid mid-Carnian episode? J. Geol. Soc. (London) 176, 133–148.

Furin, S., Preto, N., Rigo, M., Roghi, G., Gianolla, P., Crowley, J.L., Bowring, S.A., 2006. High-precision U-Pb zircon age from the Triassic of Italy: Implications for the Triassic time scale and the Carnian origin of calcareous nannoplankton, lepidosaurs, and dinosaurs. Geology 34(12), 1009–1012.

Gattolin, G., Preto, N., Breda, A., Franceschi, M., Isotton, M., Gianolla, P., 2015. Sequence stratigraphy after the demise of a high-relief carbonate platform (Carnian of the dolomites): sea-level and climate disentangled. Palaeogeogr. Palaeoclimatol. Palaeoecol. 423, 1–17.

Grimm, E.C., 2004. Tilia and Tilia. Graph V.2.0.2. Illinois State Museum, Springfield, USA.

Hornung, T., Krystin, L., Brandner, R., 2007. A Tethys-wide mid-Carnian (Upper Triassic) carbonate productivity crisis: Evidence for the Alpine Reingraben Event from Spiti (Indian Himalaya)? J. Asian Earth Sci. 30(2), 285–302.

Hounslow, M.W., Hu, M., Mørk, A., Vigran, J.O., Weitschat, W., Orchard, M.J., 2007. Magneto-biostratigraphy of the Middle to Upper Triassic transition, central Spitsbergen, arctic Norway. J. Geol. Soc. London 164, 581–597.

Jiang, H.S., Yuan, J.L., Chen, Y., Ogg, J.G., Yan, J.X., 2019. Synchronous onset of the Mid-Carnian Pluvial Episode in the East and West Tethys: Conodont evidence from Hanwang, Sichuan, South China. Palaeogeogr. Palaeoclimatol. Palaeoecol. 520, 173–180.

Jin, X., Gianolla, P., Shi, Z.Q., Franceschi, M., Caggiati, M., Du, X.Y., Preto, N., 2020. Synchronized changes in shallow water carbonate production during the Carnian Pluvial Episode (Late Triassic) throughout Tethys. Glob. Planet Change 184, 103035.

Jin, X., McRoberts, C.A., Shi, Z.Q., Mietto. P., Rigo, M., Roghi, G., Manfrin, S., Franceschi, M., Preto, N., 2019. The aftermath of the CPE and the Carnian–Norian transition in northwestern Sichuan Basin, South China. J. Geol. Soc. London 176, 179–196.

Jin, X., Shi, Z.Q., Rigo, M., Franceschi, M., Preto, N., 2018. Carbonate platform crisis in the Carnian (Late Triassic) of Hanwang (Sichuan Basin, South China): insights from conodonts and stable isotope data. J. Asian Earth Sci. 164, 104–124.

Kozur, H., Bachmann, G.H., 2010. The Middle Carnian wet intermezzo of the Stuttgart Formation (Schilfsanstein), Germanic Basin. Palaeogeogr. Palaeoclimatol. Palaeoecol. 290, 107–119.

Kustatscher, E., Ash, S.R., Karasev, E., Pott, C., Vajda, V., Yu, J.X., McLoughlin, S., 2018. Flora of the Late Triassic. In: Tanner, L.H. (Ed.), The Late Triassic World. Springer, pp. 545–622.

Kustatscher, E., Heunisch, C., Van Konijnenburg-Van Cittert, J.H.A., 2012. Taphonomical implications of the Ladinian megaflora and palynoflora of Thale

(Germany). Palaios 27, 753–764.

Li, L.Q., Wang, Y.D., Vajda, V., Liu, Z.S., 2018. Late Triassic ecosystem variations inferred by palynological records from Hechuan, southern Sichuan Basin, China. Geol. Mag. 155, 1793–1810.

Li, L.Q., Wang, Y.D., Kürschner, W.M., Ruhl, M., Vajda, V., 2020. Palaeovegetation and palaeoclimate changes across the Triassic–Jurassic transition in the Sichuan Basin, China. Palaeogeogr. Palaeoclimatol. Palaeoecol. 556, 109891.

Li, Q., Ruhl, M., Wang, Y.D., Xie, X.P., An, P.C., Xu, Y.Y., 2021. Response of Carnian Pluvial Episode evidenced by organic carbon isotopic excursions from western Hubei, South China. Palaeoworld, https://doi.org/10.1016/j.palwor.2021.08.004.

Li, Y., Su, D.H., Dong, S.L., Sun, W., Yang, R.J., Liu, S.G., Yan, Z.K., Yan, L., 2011. Dynamic of drowing of the carbonate ramp and sponge build-up in the stage (Carnian) of Longmenshan foreland basin, late Triassic, China. Acta Petrol. Sin. 27 (11), 3460–3470 (in Chinese with English abstract).

Li, Z.H., Chen, Z.Q., Zhang, T.F., Ogg, J.G., Zhao, L.S., 2020. Global carbon cycle perturbations triggered by volatile volcanism and ecosystem responses during the Carnian Pluvial Episode (late Triassic). Earth Sci. Rev. 211, 103404.

Lindström, S., 2016. Palynofloral patterns of terrestrial ecosystem change during the end-Triassic event – a review. Geol. Mag. 153, 223–251.

Lindström, S., Erlström, M., Piasecki, S., Nielsen, L.H., Mathiesen, A., 2017. Palynology and terrestrial ecosystem change of the Middle Triassic to lowermost Jurassic succession of the eastern Danish Basin. Rev. Palaeobot. Palyno. 244, 65–95.

Litwin, R.J., 1985. Fertile organs and in situ spores of ferns from the Late Triassic Chinle Formation of Arizona and New Mexico, with discussion of the associated dispersed spores. Rev. Palaeobot. Palynol. 44, 101–146.

Lu, J., Zhang, P.X., Dal Corso, J., Yang, M.F., Wignall, P.B., Greene, S.E., Shao, L.Y., Lyu, D., Hilton, J., 2021. Volcanically driven lacustrine ecosystem changes during the Carnian Pluvial Episode (Late Triassic). Proc. Natl. Acad. Sci. U.S.A. 118, e2109895118.

Lu, M.N., Wang, R.S., 1980. Discovery of microflora from the Maantang Formation in the north-west Sichuan Basin and its significance. Acta Bot. Sin. 22 (4), 370–378 (in Chinese with English abstract).

Lu, M.N., Wang, R.S., 1987. Late Triassic–Early Jurassic spore-pollen assemblages in Sichuan Basin and their distribution. In: Editorial Committee of Professional Papers of Petroleum Stratigraphy and Palaeontology (Ed.), Professional Papers of Petroleum Stratigraphy and Palaeontology. Geological Publishing House, Beijing, pp. 207–212 (in Chinese).

Mander, L., Collinson, M.E., Chaloner, W.G., Brain, A.P.R., Long, D.G., 2012. The ultrastructure and botanical affinity of the problematic mid-Mesozoic palynomorph *Ricciisporites tuberculatus* Lundblad. Int. J. Plant Sci. 173, 429–440.

Mazaheri-Johari, M., Gianolla, P., Mather, T.A., Frieling, J., Chu, D., Dal Corso, J., 2021. Mercury deposition in Western Tethys during the Carnian Pluvial Episode (Late Triassic). Sci. Rep. 11, 1–10.

Mazaheri-Johari, M., Roghi, G., Caggiati, M., Kustatscher, E., Ghasemi-Nejad, E., Zanchi, A., Gianolla, P., 2022. Disentangling climate signal from tectonic forcing: The Triassic Aghdarband Basin (Turan Domain, Iran). Palaeogeogr. Palaeoclimatol. Palaeoecol. 586, 110777.

Mietto, P., Jin, X., Manfrin, S., Lu, G., Shi, Z.Q., Gianolla, P., Huang, X.T., Preto, N., 2021. Onset of sedimentation near the Carnian/Norian boundary in the northwestern

Sichuan Basin: New evidence from ammonoid biostratigraphy and zircon U–Pb geochronology. Palaeogeogr. Palaeoclimatol. Palaeoecol. 567, 110246.

Miller, C.S., Peterse, F., da Silva, A.-C., Baranyi, V., Reichart, G.J., Kürschner, W.M., 2017. Astronomical age constraints and extinction mechanisms of the Late Triassic Carnian crisis. Sci. Rep. 7, 2557.

Mueller, S., Hounslow, M.W., Kürschner, W.M., 2016a. Integrated stratigraphy and palaeoclimate history of the Carnian Pluvial Event in the Boreal realm; new data from the Upper Triassic Kapp Toscana Group in central Spitsbergen (Norway). J. Geol. Soc. London 173, 186–202.

Mueller, S., Krystyn, L., Kürschner, W.M., 2016b. Climate variability during the Carnian Pluvial Phase — A quantitative palynological study of the Carnian sedimentary succession at Lunz am See, Northern Calcareous Alps, Austria. Palaeogeogr. Palaeoclimatol. Palaeoecol. 441, 198–211.

Nakada, R., Ogawa, K., Suzuki, N., Takahashi, S., Takahashi, Y., 2014. Late Triassic compositional changes of aeolian dusts in the pelagic Panthalassa: Response to the continental climatic change. Palaeogeogr. Palaeoclimatol. Palaeoecol. 393, 61–75.

Nowak, H., Kustatscher, E., Roghi, G., Van Konijnenburg-Van Cittert, J.H.A., 2022. Variability of *in situ* spores in some leptosporangiate ferns from the Triassic in Italy and Austria. Rev. Palaeobot. Palynol. 296, 104544.

Peng, J., Slater, S.M., Vajda, V., 2022. A Late Triassic vegetation record from the Huangshanjie Formation, Junggar Basin, China: possible evidence for the Carnian Pluvial Episode. Geo. Soc. London Special Pub. 521, in press. https://doi.org/10.1144/SP521-2021-151.

Pott, C., Krings, M., Kerp, H., 2008. The Carnian (Late Triassic) flora from Lunz in

Lower Austria: Paleoecological considerations. Palaeoworld 17, 172–182.

Preto, N., Kustatscher, E., Wignall, P.B., 2010. Triassic climates — State of the art and perspectives. Palaeogeogr. Palaeoclimatol. Palaeoecol. 290, 1–10.

Prochnow, S.J., Nordt, L.C., Archley, S.C., Hudec, M.R., 2006. Multiproxy paleosol evidence for middle and late Triassic climate trends in eastern Utah. Palaeogeogr. Palaeoclimatol. Palaeoecol. 232, 53–72.

Rigo, M., Preto, N., Roghi, G., Tateo, F., Mietto, P., 2007. A rise in the Carbonate Compensation Depth of western tethys in the Carnian (Late Triassic): Deep-water evidence for the Carnian pluvial event. Palaeogeogr. Palaeoclimatol. Palaeoecol. 246, 188–205.

Roghi, G., 2004. Palynological investigations in the Carnian of the Cave del Predil area (Julian Alps, NE Italy). Rev. Palaeobot. Palyno. 132, 1–35.

Roghi, G., Gianolla, P., Minarelli, L., Pilati, C., Preto, N., 2010. Palynological correlation of Carnian humid pulses throughout western Tethys. Palaeogeogr. Palaeoclimatol. Palaeoecol. 290, 89–10[illegible]

Rostási, Á., Raucsik, B., Varga, A., 2011. Palaeoenvironmental controls on the clay mineralogy of Carnian sections from the Transdanubian Range (Hungary). Palaeogeogr. Palaeoclimatol. Palaeoecol. 300, 101–112.

Ruffell, A., Simms, M.J., Wignall, P.B., 2016. The Carnian Humid Episode of the late Triassic: a review. Geol. Mag. 153, 271–284.

Scotese, C.R., 2014. Atlas of Middle & Late Permian and Triassic Paleogeographic Maps, map 45 from Volume 3 of the PALEOMAP Atlas for ArcGIS (Jurassic and Triassic). Mollweide Projection, PALEOMAP Project, Evanston, IL.

Shi, Z.Q., Jin, X., Preto, N., Rigo, M., Du, Y.X., Han, L., 2019. The Carnian Pluvial Episode at Ma'antang, Jiangyou in Upper Yangtze Block, Southwestern China. J. Geol. Soc. London 176, 197–207.

Shi, Z.Q., Preto, N., Jiang, H.S., Krystyn, L., Zhang, Y., Ogg, J.G., Jin, X., Yuan, J.L., Yang, X.K., Du, Y.X., 2017. Demise of Late Triassic sponge mounds along the northwestern margin of the Yangtze Block, South China: Related to the Carnian Pluvial Phase? Palaeogeogr. Palaeoclimatol. Palaeoecol. 471, 247–263.

Simms, M.J., Ruffell, A.H., 1989. Synchroneity of climatic change and extinctions in the Late Triassic. Geology 17, 265–268.

Song, Z.C., Shang, Y.K., Liu, Z.S., Huang, P., Wang, X.F., Qian, L.J., Du, B.A., Zhang, D.H., 2000. Fossil spores and pollen of China, Vol. 2. The Mesozoic spores and pollen. Science Presss, Beijing. 710pp. (in Chinese with English abstract).

Stefani, M., Furin, S., Gianolla, P., 2010. The changing climate framework and depositional dynamics of Triassic carbonate platforms from the Dolomites. Palaeogeogr. Palaeoclimatol. Palaeoecol. 290, 43–57.

Sun, G., Meng, F.S, Qian, L.J., Ouyang, S., 1995. Triassic floras. In: Lee, H.H., Zhou, Z.Y., Cai, C.Y., Sun, G., Ou, Y.S., Deng, L.H. (Eds.), Fossil Floras of China through the Geological Ages. Guangdong Science and Technology Press, Guangzhou, pp. 305–410.

Sun, Y.D., Wignall, P.B., Joachimski, M.M., Bond, D.P.G., Grasby, S.E., Lai, X.L., Wang, L.N., Zhang, Z.T., Sun, S., 2016. Climate warming, euxinia and carbon isotope perturbations during the Carnian (Triassic) Crisis in South China. Earth Planet. Sci. Lett. 444, 88–100.

Tomimatsu, Y., Nozaki, T., Sato, H., Takaya, Y., Kimura, J.-I., Chang, Q., Naraoka, H., Rigo, M., Onoue, T., 2021. Marine osmium isotope record during the Carnian "pluvial episode" (Late Triassic) in the pelagic Panthalassa Ocean. Glob. Planet. Change 197, 103387.

Van Konijnenburg-Van Cittert, J.H.A., 1971. In situ gymnosperm pollen from the Middle Jurassic of Yorkshire. Acta Bot. Neerl. 20, 1–97.

Van Konijnenburg-Van Cittert, J.H.A., 1993. A review of the Matoniaceae based on in situ spores. Rev. Palaeobot. Palynol. 78, 235–267.

Van Konijnenburg-Van Cittert, J.H.A., 2002. Ecology of some Late Triassic to Early Cretaceous ferns in Eurasia. Rev. Palaeobot. Palynol. 119, 113–124.

Van Soelen, E.E., Kürschner, W.M., 2018. Late Permian to Early Triassic changes in acritarch assemblages and morphology in the Boreal Arctic: New data from the Finnmark Platform. Palaeogeogr. Palaeoclimatol. Palaeoecol. 505, 120–127.

Visscher, H., Houte, M.V., Brugman, W.A., Poort, R.J., 1994. Rejection of a Carnian (Late Triassic) "pluvial event" in Europe. Rev. Palaeobot. Palynol. 83, 217–226.

Visscher, H., Van der Zwan, C.J., 1981. Palynology of the circum-Mediterranean Triassic phytogeographical and palaeoclimatological implications. Geol. Rundsch. 70, 625–636.

Wang, Y.D, Fu, B.H., Xie, X.P., Huang, Q.S., Li, K., Li, G., Liu, Z.S., Yu, J.X., Pan, Y.H., Tian, N., Jiang, Z.K., 2010. The terrestrial Triassic and Jurassic Systems in the Sichuan Basin, China. University of Science and Technology of China Press, Hefei. 216 pp. (in Chinese and English).

Wang, Y.D., Li, L.Q., Guignard, G., Dilcher, D.L., Xie, X.P., Tian, N., Zhou, N., Wang, Y., 2015. Fertile structures with in situ spores of a dipterid fern from the Triassic in southern China. J. Plant Res. 128, 445–457.

Wang, Y.D., Zhang, H., 2010. Fertile organs and *in situ* spores of a new dipteridaceous fern *Hausmannia sinensis* from the Jurassic of northern China. P. Roy. Soc. B-Biol. Sci. 277, 311–320.

Wu, X.C., 1984. Paleoecological characteristics of Late Triassic sponge patch reefs in north-western Sichuan, China. J. Chengdu Inst. Geol. 1, 43–54 (in Chinese with English abstract).

Wu, X.C., 1989. Carnian (Upper Triassic) sponge mounds of the northwestern Sichuan basin, China: stratigraphy, facies and paleoecology. Facies 21, 171–188.

Zhang, Y., Li, M.S., Ogg, J.G., Montgomery, P., Huang, C.J., Chen, Z.Q., Shi, Z.Q., Enos, P., Lehrmann, D.J., 2015. Cycle-calibrated magnetostratigraphy of middle Carnian from South China: Implications for Late Triassic time scale and termination of the Yangtze Platform. Palaeogeogr. Palaeoclimatol. Palaeoecol. 436, 135–166.

Zhou, T., Zhou, H., 1983. Triassic non-marine strata and flora of China. Bulletin Chinese Acad. Geol. Sci. 5, 95–108 (in Chinese with English abstract).

Legends of figures, table and supplementary table

Figures

Fig. 1 Location of the Ma'antang section at northwestern Sichuan Basin and geological map of the study area. A) Palaeogeographic map of the Carnian (Late Triassic) indicating the study area (modified from Scotese, 2014); B) Geographic range of the Sichuan Basin showing the study area; C) Geological map of the Ma'antang section and adjacent area.

Fig. 2 Lithological column and relative abundance of spore and pollen genera of the Upper Triassic Ma'antang Formation, at the Ma'antang section. The lithology, geological age frame follows Shi et al. (2019).

Fig. 3 Palaeovegetation composition of the Ma'antang Formation at the Ma'antang section.

Fig. 4 Relative abundance of sporomorphs ecogroups, and hygrophyte-xerophyte sporopollen of the Ma'antang Formation at the Ma'antang section.

Fig. 5 Correlation of the carbon-isotope records and palaeoclimate proxies between eastern and western Tethys during the Carnian Pluvial Episode (CPE). H/X ratio: hygrophyte/xerophyte ratio.

Plate I. Representative azonotrilete spores of the Ma'antang Formation at Ma'antang section. 1) *Sphagnumsporites perforatus* (Leschik) Liu 1986, MAT-16; 2-3) *Dictyophyllidites charicis* Zhang 1984, 2. MAT-2, 3. MAT-23; 4. *Dictyophyllidites intercrassus* Ouyang et Li 1980, MAT-11; 5-6) *Dictyophyllidites harrisii* Couper 1958, 5. MAT-2, 6. MAT-15; 7-8) *Dictyophyllidites mortoni* (De Jersey) Playford et Dettmann 1965, MAT-2; 9-10) *Concavisporites bohemiensis* Thiergart 1953, 9. MAT-12, 10. MAT-13; 11-13) *Concavisporites toralis* (Leschik 1955) Nilsson 1958, 11, 13. MAT-2, 13. MAT-3; 14-15) *Granulatisporites parvus* (Ibrahim) Potonié et Kremp 1955, 14. MAT-13, 15. MAT-11; 16-17) *Granulatisporites granulatus* Ibrahim 1933, 16. MAT-3, 17. MAT-19; 18-19) *Lunzisporites delicatulus* Shang 1981, 18. MAT-14, 19. MAT-11; 20) *Osmundacidites parvus* De Jersey 1962, MAT-17; 21-22) *Lunzisporites lunzensis* Bharadwaj et Singh 1964, 21. MAT-17, 22. MAT-17; 23) *Angiopteridaspora denticulata* Chang 1965, MAT-17; 24) *Conbaculatisporites pauculus* Bai et Lu 1983, MAT-18; 25) *Baculatisporites comaumensis* (Cookson) Potonié 1956, MAT-16; 26) *Conbaculatisporites mesozoicus* Klaus 1960, MAT-17; 27-28) *Uvaesporites minisculus* Lu et Wang 1980, 27. MAT-2, 28. MAT-3; 29) *Lycopodiacidites minus* Lu et Wang 1980, MAT-14. Scale bar is 20 μm.

Plate II. Representative zonotrilete and monolete spores of the Ma'antang Formation at Ma'antang section. 1-4) *Kyrtomisporis laevigatus* Mädler 1964, 1-2. MAT-3, 3-4. MAT-4; 5-8) *Kyrtomisporis coronarius* (Chang) Li et Shang 1980, MAT-4; 9) *Kyrtomisporis speciosus* Mädler 1964, MAT-4; 10) *Asseretospora gyrata* (Playford et Dettmann) Schuurman 1977, MAT-2; 11) *Annulispora folliculosa* (Rogalska) De Jersey 1959, MAT-

2; 12) *Polycingulatisporites tenuis* Shang et Li 1991, MAT-4; 13) *Canalizonospora canaliculata* Li 1974, MAT-2; 14) *Camarozonosporites rudis* (Leschik) Klaus 1960, MAT-12; 15) *Kraeuselisporites linearis* (Cookson et Dettmann) Dettmann 1963, MAT-4; 16) *Laevigatosporites ovatus* Wilson et Webster 1946, MAT-18. Scale bar is 20 μm.

Plate III. Representative pollen and aquatic palynomorphs of the Ma'antang Formation at Ma'antang section. 1) *Lueckisporites triassicus* Clarke 1965, MAT-23; 2) *Protohaploxypinus* sp., MAT-17; 3) *Granosaccus ornatus* (Pautsch) Pautsch 1973, MAT-2; 4-5) *Verrusaccus sichuanensis* Lu et Wang 1990, 4. MAT-23, 5. MAT-2; 6) *Alisporites parvus* De Jersey 1962, MAT-23; 7) *Pinuspollenites divulgatus* (Bolkh.) Qu 1980, MAT-19; 8) *Chasmatosporites major* Nilsson 1958, MAT-2; 9) *Ovalipollis ovalis* Krutzsch 1955, MAT-13; 10) *Cycadopites follicularis* Wilson et Webster 1946, MAT-19; 11) *Cycadopites granulatus* (De Jersey) De Jersey 1964, MAT-14; 12) *Ricciisporites tuberculatus* Lundblad 1954, MAT-4; 13-14) *Caytonipollenites pallidus* (Reissinger) Couper 1958, 13. MAT-15, 14. MAT-17; 15) *Veryhachium* sp., MAT-2; 16-17) *Micrhystridium* sp., 16. MAT-3, 17. MAT-2; 18) *Baltisphaeridium* sp. MAT-2; 19) Foraminiferal test lining, MAT-14. Scale bar is 20 μm.

Table

Table 1. Botanical affinity, SEG and ecological remarks of the identified spores and pollen at the Ma'antang Section, Jiangyou of Sichuan, SW China.

Supplementary table

Table S1. Original palynological data of the Ma'antang Formation from the Ma'antang Section, Jiangyou of Sichuan, SW China.

Table 1. Botanical affinity, SEG and ecological remarks of the identified spores and pollen at the Ma'antang Section, Jiangyou of Sichuan, SW China

Sporo-pollen genera	Botanical affinity	SEGs	Ecology
Concavisporites	fern (Dipteridaceae/Matoniaceae)	wet Lowland	hygrophyte
Dictyophyllidites	fern (Dipteridaceae/Matoniaceae)	wet Lowland	hygrophyte
Cyathidites	fern (Dipteridaceae/Dicksoniaceae)	wet Lowland	hygrophyte
Deltoidospora	fern (Dipteridaceae/Dicksoniaceae)	wet Lowland	hygrophyte
Granulatisporites	fern (Dipteridaceae)	wet Lowland	hygrophyte
Lunzisporites	fern (Dipteridaceae)	wet Lowland	hygrophyte
Conbaculatisporites	fern (Dipteridaceae)	wet Lowland	hygrophyte
Baculatisporites	fern (Osmundaceae/Dipteridaceae)	wet Lowland	hygrophyte
Biretisporites	fern (Osmundaceae)	wet Lowland	hygrophyte
Osmundacidites	fern (Osmundaceae)	wet Lowland	hygrophyte
Punctatisporites	fern (Osmundaceae/Marattiales)	wet Lowland	hygrophyte
Cyclogranisporites	fern (Osmundaceae/Marattiales)	wet Lowland	hygrophyte
Angiopteridaspora	fern (Marattiales)	wet Lowland	hygrophyte
Marattisporites	fern (Marattiales)	wet Lowland	hygrophyte
Laevigatosporites	fern (Marattiales)	wet Lowland	hygrophyte
Asseretospora	fern (Pteridaceae)	wet Lowland	hygrophyte
Planisporites	fern	wet Lowland	hygrophyte
Klukisporites	fern	wet Lowland	hygrophyte
Canalizonospora	fern	wet Lowland	hygrophyte
Kyrtomisporis	fern	wet Lowland	hygrophyte
Habrozonosporites	fern	wet Lowland	hygrophyte
Araucariacites	conifer (Araucariaceae)	wet Lowland	intermediate
Cerebropollenites	conifer (Taxodiaceae)	wet Lowland	intermediate
Monosulcites	cycadophytes/ginkgophytes	dry Lowland	intermediate
Chasmatosporites	cycadophytes/ginkgophytes	dry Lowland	intermediate
Cycadopites	cycadophytes/ginkgophytes	dry Lowland	intermediate

Caytonipollenites	seed fern	River	hygrophyte?
Alisporites	seed fern	River	hygrophyte?
Protohaploxypinus	seed fern	River	hygrophyte?
Calamospora	horsetail	River	hygrophyte
Anapiculatisporites	lycopsid	River	hygrophyte
Acanthotriletes	lycopsid	River	hygrophyte
Neoraistrickia	lycopsid	River	hygrophyte
Leptolepidites	lycopsid	River	hygrophyte
Uvaesporites	lycopsid	River	hygrophyte
Lycopodiacidites	lycopsid	River	hygrophyte
Lycodiumsporites	lycopsid	River	hygrophyte
Camarozonosporites	lycopsid	River	hygrophyte
Densoisporites	lycopsid	River	hygrophyte
Kraeuselisporites	lycopsid	River	hygrophyte
Aratrisporites	lycopsid	River	hygrophyte
Sphagnumsporites	moss	River	hygrophyte
Annulispora	moss	River	hygrophyte
Polycingulatisporites	moss	River	hygrophyte
Limatulasporites	moss	River	hygrophyte
Pinuspollenites	conifer (Pinaceae)	Hinterland	xerophyte
Cedripites	conifer (Pinaceae)	Hinterland	xerophyte
Taeniaesporites	conifer (Podocarpaceae)	Hinterland	xerophyte
Quadraeculina	conifer (Podocarpaceae)	Hinterland	xerophyte
Podocarpidites	conifer (Podocarpaceae)	Hinterland	xerophyte
Protopinus	conifer (Podocarpaceae)	Hinterland	xerophyte
Paleoconiferus	conifer (Podocarpaceae)	Hinterland	xerophyte
Protopodocarpus	conifer (Podocarpaceae)	Hinterland	xerophyte
Piceites	conifer (Podocarpaceae)	Hinterland	xerophyte
Protopicea	conifer (Podocarpaceae)	Hinterland	xerophyte

Ovalipollis	conifer (Voltziales)	Hinterland	intermediate
Lueckisporites	conifer	Hinterland	xerophyte
Granosaccus	conifer	Hinterland	xerophyte
Verrusaccus	conifer	Hinterland	xerophyte
Ricciisporites	indetermined gymnosperm	NA	NA

NA=not attributed.

Declaration of interests

☒The authors declare that they have no known competing financial interests or personal relationships that could have appeared to influence the work reported in this paper.

☐The authors declare the following financial interests/personal relationships which may be considered as potential competing interests:

Highlights

First quantitative CPE palynological data from South China

Palynological analysis reveal increased humidity during the Julian 2 in western Sichuan Basin

Correlation between eastern and western Tethys based on the palynological and carbon isotope data

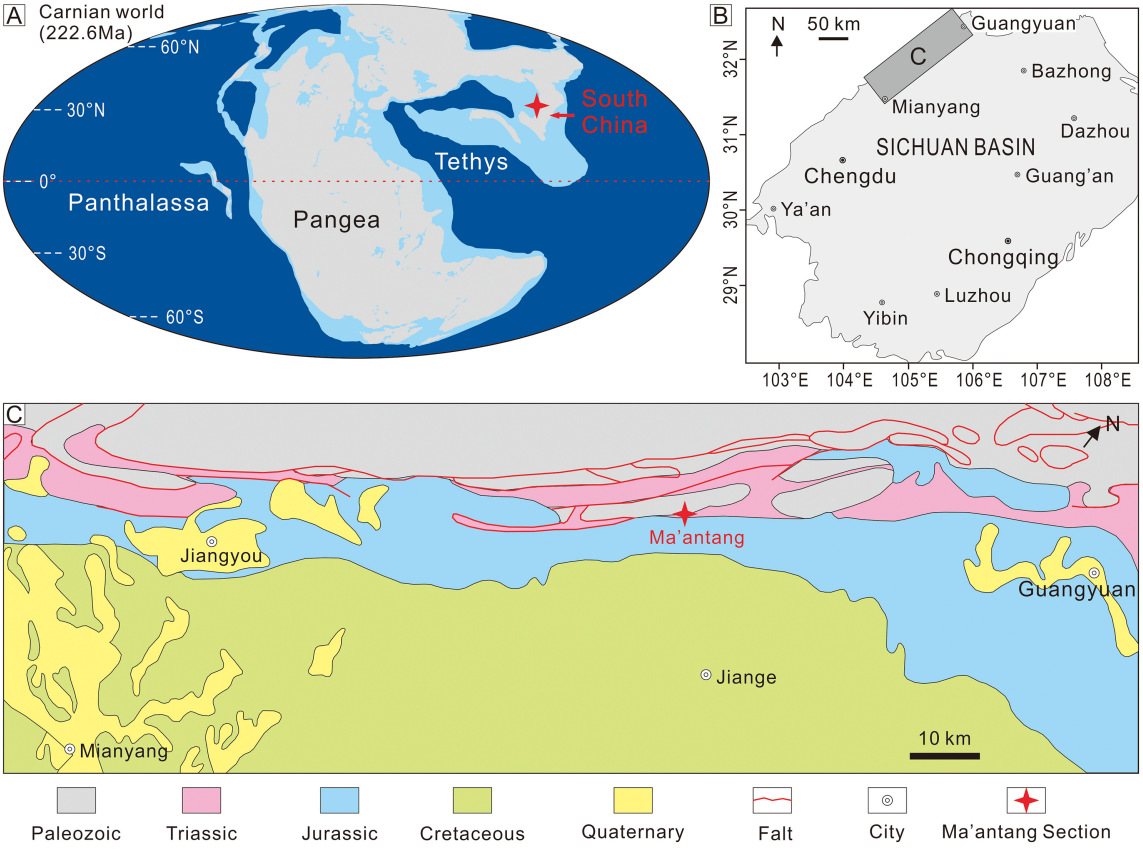
A
Carnian world
(222.6Ma)
60°N
30°N
0°
30°S
60°S
South
China
Tethys
Panthalassa
Pangea
B
N
50 km
C
Guangyuan
Bazhong
Mianyang
Dazhou
SICHUAN BASIN
Chengdu
Guang'an
Ya'an
Chongqing
Luzhou
Yibin
32°N
31°N
30°N
29°N
103°E
104°E
105°E
106°E
107°E
108°E
C
N
Ma'antang
Jiangyou
Guangyuan
Jiange
Mianyang
10 km
Paleozoic
Triassic
Jurassic
Cretaceous
Quaternary
Falt
City
Ma'antang Section

Figure 1

Terrestrial sporomorph
Spores
Pollen
Cyathidites
Deltoidospora
Punctatisporites
Concavisporites
Dictyophyllidites
Granulatisporites
Cyclogranisporites
Osmundacidites
Uvaesporites
Planisporites
Lunzisporites
Angiopteridaspora
Annulispora
Asseretospora
Kyrtomisporis
Canalizonospora
Kraeuselisporites
Taeniaesporites
Lueckisporites
Caytonipollenites
Alisporites
Pinuspollenites
Podocarpidites
Araucariacites
Ovalipollis
Ricciisporites
Chasmatosporites
Cycadopites
Terrestrial sporomorph
Aquatic sporomorph
CONISS
Palynological assemblages
Samples
MAT-23
MAT-22
MAT-21
MAT-20
MAT-19
MAT-18
MAT-17
MAT-16
MAT-15
MAT-14
MAT-13
MAT-12
MAT-11
MAT-10
MAT-9
MAT-8
MAT-7
MAT-6
MAT-5
MAT-4
MAT-3
MAT-2
MAT-1
Carnian
Ladinian
Julian 2
Tuvalian
Norian
Juli. 1
Xiaotangzi
Tianjingshan
Ma'antang Formation
Unit 1
Unit 2
Unit 3
Unit 4
Unit 5
A
B
20m
10
20
20 40
20 40
20
20 40
20
50 100
1 2 3 4
Total sum of squares
[Relative abundance (%)]
karst surface
limestone
conglomerate
sandstone
muddy siltstone
silty mudstone
samples
productive samples

Figure 2

Age
Fm.
Units
Carnian
Julian 2
Tuvalian
Juli. 1
Ma'antang Formation
Unit 1
Unit 2
Unit 3
Unit 4
Unit 5
Ferns
Cycadophytes /ginkgophytes
Seed ferns
Horsetails
Lycopsids
Conifers
Mosses
Indetermined gymnosperms
20
40
60
80
100
[Percentages%]
Dipteridaceae /Matoniaceae
Osmundaceae
Marattiales
Pteridaceae
Other ferns
40
80
10
40
Ferns

Figure 3

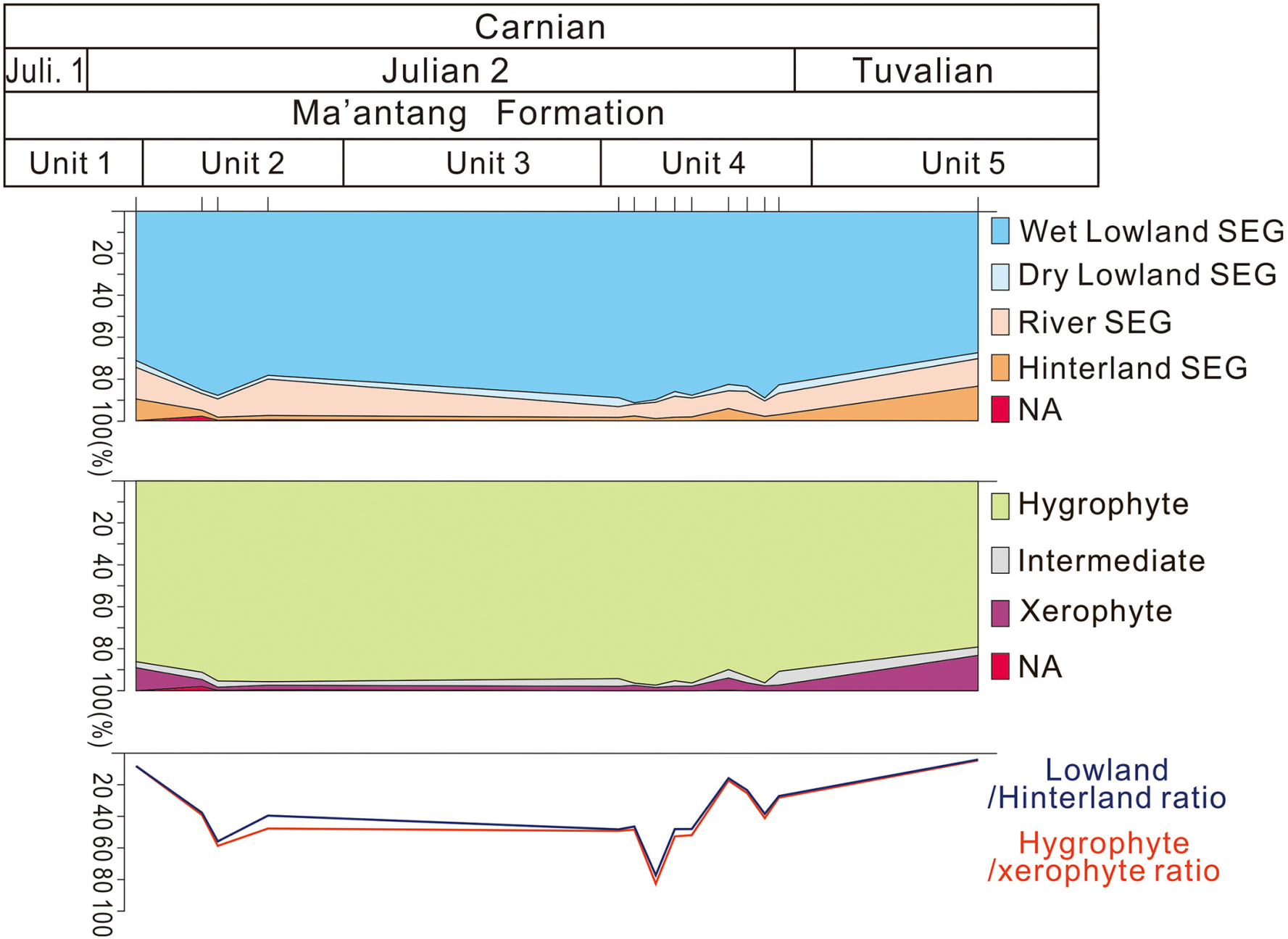
Carnian
Juli. 1
Julian 2
Tuvalian
Ma'antang Formation
Unit 1
Unit 2
Unit 3
Unit 4
Unit 5
20 40 60 80 100(%)
Wet Lowland SEG
Dry Lowland SEG
River SEG
Hinterland SEG
NA
20 40 60 80 100(%)
Hygrophyte
Intermediate
Xerophyte
NA
20 40 60 80 100
Lowland /Hinterland ratio
Hygrophyte /xerophyte ratio

Figure 4

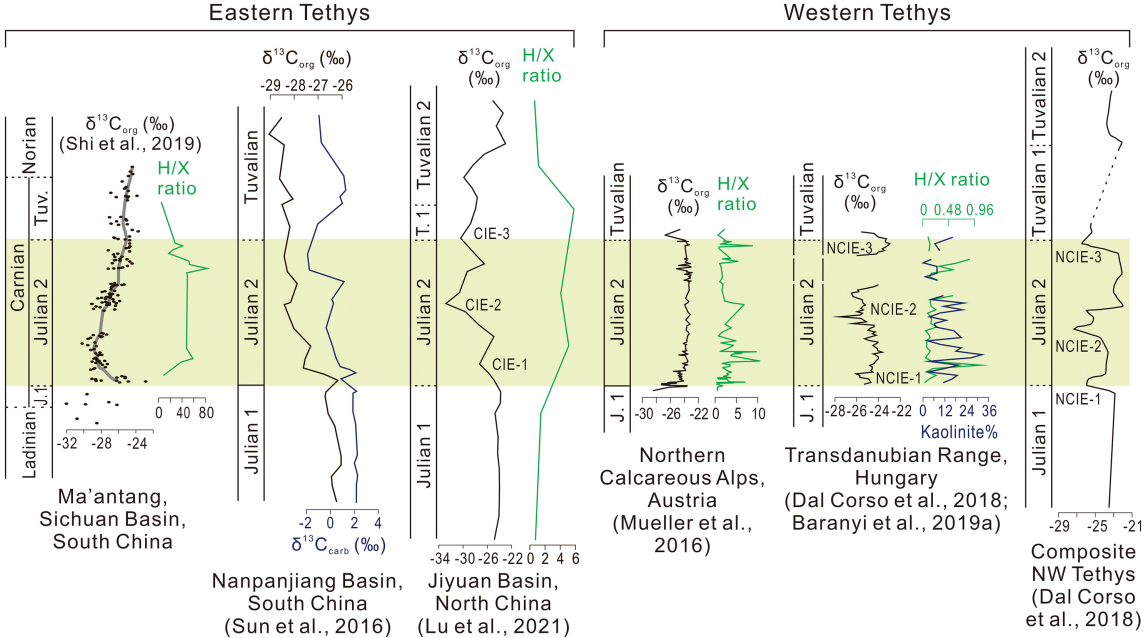
Eastern Tethys
Western Tethys
Norian
Tuv.
Carnian
Julian 2
J. 1
Ladinian
δ13Corg (‰)
(Shi et al., 2019)
H/X ratio
0 40 80
-32 -28 -24
Ma'antang, Sichuan Basin, South China
δ13Corg (‰)
-29 -28 -27 -26
Tuvalian
Julian 2
Julian 1
-2 0 2 4
δ13Ccarb (‰)
Nanpanjiang Basin, South China (Sun et al., 2016)
δ13Corg (‰)
H/X ratio
T. 1
Tuvalian 2
CIE-3
CIE-2
CIE-1
-34 -30 -26 -22 0 2 4 6
Jiyuan Basin, North China (Lu et al., 2021)
Tuvalian
Julian 2
J. 1
δ13Corg (‰)
H/X ratio
-30 -26 -22 0 5 10
Northern Calcareous Alps, Austria (Mueller et al., 2016)
Tuvalian
Julian 2
J. 1
δ13Corg (‰)
H/X ratio
0 0.48 0.96
NCIE-3
NCIE-2
NCIE-1
-28 -26 -24 -22 0 12 24 36
Kaolinite%
Transdanubian Range, Hungary (Dal Corso et al., 2018; Baranyi et al., 2019a)
Tuvalian 1
Tuvalian 2
Julian 2
Julian 1
δ13Corg (‰)
NCIE-3
NCIE-2
NCIE-1
-29 -25 -21
Composite NW Tethys (Dal Corso et al., 2018)

Figure 5